

The First Detection of [O IV] from an Ultraluminous X-ray Source with *Spitzer*: Evidence of High Unbeamed Luminosity in Holmberg II ULX

C. T. Berghea

Physics Department, The Catholic University of America, Washington, DC 20064

79berghea@cua.edu

R. P. Dudik^{1,2}

United States Naval Observatory, Washington, DC 20392

rpudik@usno.navy.mil

K. A. Weaver and T. R. Kallman

Laboratory for High Energy Astrophysics, NASA Goddard Space Flight Center, Greenbelt, MD 20771

ABSTRACT

We present the first *Spitzer* Infrared Spectrograph (IRS) observations of the [O IV] 25.89 μm emission line detected from the ultraluminous X-ray source (ULX) in Holmberg II. This line is a well established signature of high excitation, usually associated with AGN. Its detection suggests that the ULX has a strong impact on the surrounding gas. A *Spitzer* high resolution spectral map shows that the [O IV] is coincident with the X-ray position of the Holmberg II ULX. We find that the luminosity and the morphology of the line emission is consistent with photoionization by the soft X-ray and far ultraviolet (FUV) radiation from the accretion disk of the binary system and inconsistent with narrow beaming. We show that the emission nebula is radiation bounded both in the line of sight direction and to the west, and probably matter bounded to the east. Evidence for a massive black hole (BH) in this ULX is mounting. Detailed photoionization

¹Observational Cosmology Lab, NASA Goddard Space Flight Center, Greenbelt, MD 20771

²Department of Physics & Astronomy, George Mason University, Fairfax, VA 22030; rachel@physics.gmu.edu

models favor an intermediate mass black hole of at least $85 M_{\odot}$ as the ionization source for the [O IV] emission. We find that the spectral type of the companion star strongly affects the expected strength of the [OIV] emission. This finding could explain the origin of [OIV] in some starburst galaxies containing black hole binaries.

Subject headings: black hole physics — galaxies: individual (Holmberg II) — infrared: ISM — X-rays: binaries

1. INTRODUCTION

The majority of our knowledge of ultraluminous X-ray sources (ULXs) stems from over 200 observations of these objects by both *Chandra* and *XMM-Newton* (Liu & Mirabel 2005). The high X-ray luminosities of these sources have raised intriguing questions about their nature. A natural explanation for these luminosities is the presence of intermediate-mass black holes (IMBH, e.g. Colbert & Mushotzky 1999); however substantiating evidence for this scenario is lacking (Stobbart et al. 2006; Gonçalves & Soria 2006; Berghea et al. 2008). Attention has switched to less exotic models, such as beaming (King et al. 2001) or super-Eddington accretion (Begelman 2002), both of which explain ULX X-ray properties without an IMBH. Galactic super-Eddington sources are known, such as GRS 1915+105 (Fender & Belloni 2004), V4641 Sgr (Revnivtsev et al. 2002) and possibly SS 433. The latter could be an example of both beaming *and* super-Eddington accretion, the combination of which could easily explain even the most luminous ULXs (Begelman et al. 2006; Poutanen et al. 2007).

Very little work has been done on ULXs at non X-ray wavelengths, especially in comparison with AGN and Galactic stellar-mass black holes. This is in part because, unlike standard AGN, the emission from the accretion process itself is harder to detect at these wavelengths. Indeed, the X-ray to optical luminosity ratios in ULXs are at least ten times higher compared to those seen in AGN (Winter et al. 2007). To make matters worse, there are no ULXs in our own Galaxy (though SS 433 is regarded as a ULX by some authors), and the stellar ULX companions are very difficult to identify in other galaxies.

What little multi-wavelength work done on ULXs thus far has been executed primarily with high resolution optical spectroscopy. In a few cases, ULXs have been found to have an observable effect on their local environment. $H\alpha$ images show ionized bubble nebulae of up to 500 pc diameter around some objects (Pakull & Mirioni 2002). The ionized bubbles are much larger than regular supernova remnants and energy estimates show that the bubbles are consistent with being blown either by relativistic jets from a ULX, or abnormally

powerful supernovae. In some cases high ionization lines have been detected (e.g. He II $\lambda 4686$ Abolmasov et al. 2007). Only very hot Wolf-Rayet stars can produce these line, but the companions are not such stars. Therefore, the detection of the He II line must be due to the interaction of the ULX with the surrounding medium. Interestingly, SS 433 is also surrounded by a 100 pc radio nebula, W 50 (e.g. Fabrika 2004).

The importance of ionization nebulae for investigating X-ray sources has long been realized, beginning with the first detection of nebulae around supersoft sources such as LMC X-1 (Pakull & Angebault 1986) and CAL 83 (Remillard et al. 1995) in the Large Magellanic Cloud (LMC). The high excitation lines observed in nebulae, such as the He II recombination line, can act as giant bolometers for the ionizing UV and X-ray emission, thus allowing the intrinsic hard spectral energy distribution (SED) to be inferred. Long-term averaged luminosities can be estimated and the UV emission constrained. This provides tremendous value when studying the nature of ambiguous ULXs, because the luminosities estimated from ionization are independent of sometimes confusing X-ray spectral modeling estimates. In fact, such luminosities are more accurate, because the X-ray-based estimates are in general lower limits and depend on the viewing angle. More importantly, the ionization-estimated luminosities are time-averaged estimates, which is critical for variable sources such as ULXs, especially those with very few X-ray observations, because some ULXs could be transient.

One of the most interesting examples of an ionized nebula associated with a ULX is located in the dwarf galaxy Holmberg II (Pakull & Mirioni 2002; Lehmann et al. 2005; Abolmasov et al. 2007). He II is detected in a small nebular region around the ULX, the “Heel” of the “Foot Nebula” shown in Figure 1 (Kaaret et al. 2004, KWZ hereafter). An OB star is the likely counterpart (KWZ). The morphology of the distribution of He II emission and other optical lines is consistent with the photoionization of the nebula by the ULX. KWZ confirmed this with Cloudy simulations. Extended radio emission is also detected from a ~ 50 pc region coincident with the position of the ULX (Miller et al. 2005). The flux and morphology of the radio emission is consistent with a ULX interpretation and inconsistent with emission from a SNR or an H II region.

In this paper we use IR *Spitzer* spectroscopic observations for the first time, to constrain the underlying hard SED of a ULX. The IR observations, when combined with previously published optical and X-ray data, confirm that the powerful UV and soft X-ray emission from the Holmberg II ULX photoionizes the surrounding medium and establish the power of IR spectroscopy for studying ULXs. We use a spectral map of the high excitation line of [O IV] to estimate the time-averaged true luminosity of the ULX. In Section 2 we present the *Spitzer* IRS data analysis and additional photometry measurements with the Infrared Array Camera (IRAC), the Multiband Imaging Photometer for Spitzer (MIPS), the European

Photon Imaging Camera (EPIC) and Optical Monitor (OM) instruments on *XMM-Newton*, and the Galaxy Evolution Explorer (GALEX). In Section 3 we use our data and other published data to construct a SED of the Holmberg II ULX. We assume this SED as the ionizing source in the photoionization simulations in Section 4. In Section 5 we investigate shock models as an alternative, and in Section 6 we present some observational results. Finally, in Section 7 we present a summary of all results.

2. DATA ANALYSIS

2.1. Analysis of *Spitzer* IRS Observations

The data presented here are archival *Spitzer* data from the Legacy Program *Infrared Nearby Galaxies Survey* (SINGS Program 193, see Kennicutt et al. 2003). The IRS spectral map is described by three parallel pointings and five perpendicular at half-slit steps, for both Short High (SH, in the range 9.9-19.6 μm) and Long High (LH, in the range 18.7-37.2 μm) modules. The total exposure time was 240s for both SH and LH observations. The data were preprocessed by the IRS pipeline (version 11) at the *Spitzer* Science Center prior to download. Spectral maps were constructed using “BCD-level” processed data in conjunction with CUBISM version 1.5¹ (Kennicutt et al. 2003; Smith et al. 2004). The absolute calibration error on fluxes obtained with CUBISM is $\sim 25\%$ (Smith et al. 2004).

We adopt a distance of 3.05 Mpc to Holmberg II (KWZ, 1'' is 15 pc). The LH maps obtained with CUBISM have sizes of 44.6'' by 28.8'' (670 pc by 430 pc), while the SH maps are 27'' by 13.6'' (405 pc by 205 pc). Spectra were extracted from two different sized apertures for both the SH and LH observations. The first aperture is the maximum common aperture for LH and SH observations (see Figure 2), which is just slightly smaller than the whole SH aperture: 23'' by 13.6'' (340 pc by 205 pc). This aperture is referred to as the SH aperture throughout this paper. We also extract spectra from the smallest aperture allowed by the instrument: the four LH pixels centered on the ULX position (8.9'' by 8.9'', or 130 pc by 130 pc).

The high-resolution spectrum (10 μm –37 μm) for the Holmberg II ULX is plotted in Figure 3. Since the spectra are extracted from matched apertures, the spectral lines in both the SH and LH modules are properly calibrated and the continuum is properly matched. We also plot the spectrum from our smallest aperture in the right panel and the spectrum from the 4 LH pixels just south of this aperture for comparison.

¹Available at: <http://ssc.spitzer.caltech.edu/archanaly/contributed/cubism/>

The SH and LH maps for the detected lines are shown in Figure 2, together with the $8\ \mu\text{m}$ IRAC image. While emission from the low excitation lines [Si II] and [S III] is very extended, the [O IV] emission is clearly coincident with the *Chandra* position for the ULX. Indeed, the majority of the emission is concentrated in the 2×2 pixel region, a size that is comparable to the full width at half maximum (FWHM) of the point spread function (PSF) for these maps. However there is a slight extension to the west and south that is clearly visible on the map and which may imply that the [OIV] emission is slightly extended. KWZ found that the He II line is also concentrated in a small region of 50 pc diameter around the identified optical counterpart. Because the spatial resolution is limited, a detailed comparison of our maps with the optical maps presented in KWZ cannot be made. However, we find that the morphology of our [O IV] nebula appears similar to He II, being brighter in the east and fainter and more extended in the west. The [O IV] line is detected at a signal-to-noise ratio of 10.

Some of the [Ne III] emission may also be associated with the ULX, but it is difficult to disentangle this emission from a bright star close to the northern edge of the SH map (see the Hubble and IRAC images in Figure 1), and from the other stars west of the ULX. The former is a foreground 15th magnitude star according to both USNO and GSC catalogs. The [S III] $18.71\ \mu\text{m}$ also shows significant emission west of the ULX, but is likely not related to the ULX. The $33.48\ \mu\text{m}$ [S III] line is not detected in our observations, though it should theoretically be stronger than the $18.71\ \mu\text{m}$ [S III] line. This is likely due to the poor sensitivity of the LH observations compared to the SH. Line fluxes and upper limits are presented in Table 1.

2.2. Analysis of *Spitzer* Photometric Observations

IRAC and MIPS images (see Figs. 1 and 2) were taken as a part of SINGS Program 195 and are presented here for the purposes of constructing a detailed SED for the Holmberg II ULX. We extracted 3.6, 8.0, and $24\ \mu\text{m}$ photometric fluxes using 50 pc diameter apertures centered on the ULX position. We followed the standard extraction procedure and conversion factors provided in the *IRAC Data Handbook*². We measured 0.15 mJy and 0.26 mJy for IRAC 3.6 μm and 8.0 μm filters, respectively. The MIPS $24\ \mu\text{m}$ flux was measured to be 2.75 mJy. Since these values represent the integrated flux within the 50 pc region, which is contaminated by other stars, we treat them here as upper limits. The pipeline mosaics for IRAC and MIPS are accurate to within 20%.

²<http://ssc.spitzer.caltech.edu/irac/dh/>

2.3. UV Photometry

XMM-Newton Optical Monitor images of Holmberg II are available in the UVW1 band, which is centered at 2910Å. We use the mosaicked images created for the Optical Monitor Catalog (OMCat, Kuntz et al. 2008), which have an improved coordinate correction (better than 0.5'') over the automated pipeline. To measure the UVW1 count rate from a 50 pc diameter aperture centered on the ULX position we used the *XIMAGE* software included in the *HEAsoft* package. We converted the count rate into flux using the conversion factors listed in the *XMM-Newton Science Analysis System User's Guide*³. We obtain a UVW1 magnitude of 18.42 ± 0.06 , which corresponds to a luminosity of 8.3×10^{37} erg s⁻¹ and a flux density of 33.1 ± 0.1 μJy.

Figure 1 shows that the Foot Nebula has strong UV emission from the small cluster seen in the Hubble 814W filter image. The total UVW1 flux (including the ULX and its optical counterpart) is equivalent to 29 O5V stars. An Hα image shows that some of these bright stars have apparently blown a cavity in the NW part of the nebula. The wide-band Hubble image shows nebular emission spread across the Foot Nebula including a spherically shaped continuum, ~40 pc in diameter around the ULX.

We also used archived GALEX images of Holmberg II for the purposes of constructing a detailed SED. These observations were taken as a part of the GALEX Nearby Galaxies Survey (NGS, Bianchi et al. 2006). Photometric fluxes were extracted from the FUV (1350–2013 Å) and NUV (1750–2013 Å) bands from 50 pc apertures with the *XIMAGE* tool. We obtain fluxes of 33.7 ± 0.3 μJy and 26.3 ± 0.2 μJy for the FUV and NUV bands, respectively.

2.4. X-ray Model Fitting:

X-ray observations of the Holmberg II galaxy are available from *ROSAT*, *ASCA*, *XMM-Newton* and *Chandra* (Zezas et al. 1999; Miyaji et al. 2001; Kerp et al. 2002; Kaaret et al. 2004; Goad et al. 2006). The X-ray luminosity of the ULX is in excess of 10^{40} erg s⁻¹ in all observations, with the exception of a peculiar low and soft state in September 2002, when the luminosity dropped to $\sim 5 \times 10^{39}$ erg s⁻¹ (Dewangan et al. 2004).

To model the X-ray spectrum we used the best available data from the longest (~100 ks) *XMM-Newton* EPIC PN observation in the archive (Obs. ID 0200470101). The data were processed by Winter et al. (2006). We used XSPEC version 12.4 to model the spectrum

³http://xmm2.esac.esa.int/external/xmm_user_support/documentation/

between 0.3 and 10.0 keV. The X-ray spectrum is the most important component of the total SED since it is the only observed emission that directly emanates from the ULX, and not contaminated by the surrounding star-forming region. For this reason we have taken many precautions in modeling the X-ray spectrum. Here we discuss three models used to construct the full SED in the next section.

The below models are extrapolated to the UV and used as the primary source spectrum for photoionization in our Cloudy modeling (Section 3). The intrinsic (unabsorbed) X-ray luminosity is $>10^{40}$ erg s $^{-1}$ for all models. The results from the X-ray spectral fits are listed in Table 1, and a summary is as follows:

1. Power-law Plus Multicolor Disk (PLMCD) Model: The X-ray spectra were first fitted using a two-component model with a multicolor accretion disk component (MCD, Mitsuda, et al. 1984) and a power-law for the hard tail. Following KWZ, the absorption column density was fixed at the Galactic value of 3.42×10^{20} cm $^{-2}$, and an additional local absorption (N_H) model was added. We assume a metallicity of $0.1 Z_\odot$ (see Kaaret et al. 2004; Pilyugin et al. 2004) if not otherwise specified. The model is shown in Figure 5 (red, dashed), extrapolated to the [O IV] edge, together with the X-ray data. The PLMCD model is used universally for modeling the X-ray spectra of ULXs. In this model the power-law dominates at low energies and the MCD flux is only 12% of the total flux, (see the last column of Table 1). It will dominate even more if extrapolated to energies below 0.1 keV (i.e. into the UV). The intrinsic luminosity predicted by the PLMCD model is the largest of the three.

2. Modified PLMCD Model: The intrinsic shape of the FUV to soft X-ray SED from the accretion disk is critical to photoionization modeling. If the power-law component in the PLMCD model represents the Comptonized photons from the accretion disk emission, it cannot dominate the emission below the energies of the photons in the disk component (MCD). Therefore in order to isolate the intrinsic disk emission from the Comptonized disk emission, we also fitted the MCD and power-law separately for two different regions of the X-ray spectrum. We first fitted the hard tail with a power-law. The spectrum departs from this power-law around ~ 1 keV. Then we fitted an MCD model to the 0.3–1.0 keV band. The results are shown in Table 1. The disk temperature (0.38 keV) is slightly higher than published fits (KWZ obtained ~ 0.2 keV), because our fitting methods are slightly different. Lower temperature accretion disks are generally more effective ionizing sources, therefore this model can be viewed as a lower-limit to the FUV to soft-Xray SED (see Fig. 5).

We note that the Modified PLMCD differs from the PLMCD model in that the UV band is predicted from the MCD model rather than a MCD+PL extrapolation. In the next section we will use the Modified PLMCD model extrapolated into UV, together with the

available data at lower wavelengths, to construct the total SED. We will refer to this SED as the “base model”, and will be used as the incident Cloudy spectrum for the preliminary simulations in Section 4.1.

3. Broken Power-Law Model: We also fitted the X-ray spectrum to a family of broken power-laws. We constrained the break energy to 1.0 keV, the same energy at which the MCD and power-law component deviated in the Modified PLMCD model (2 above). The family of broken power-law models were obtained by varying the Γ_1 parameter to procure fits that were all compatible with the data within the errors ($1.3 < \Gamma_1 < 2.2$). The resulting absorption column densities vary between 2.3 and $9.2 \times 10^{20} \text{ cm}^{-2}$. We plot the limits and the best fit (BFBP hereafter, $\Gamma_1 = 1.73$) of this family of broken power-law models in Figure 6. The results for the BFBP model are shown in Table 1. Surprisingly, this simple model provides an excellent fit, better than the PLMCD model. The broken power-law model will be used to test the matter-bounded geometry in Cloudy, because with this model the column densities can be varied.

2.5. Archival Data

In addition to the photometric data presented here, we searched the literature for published data for the Holmberg II ULX at other wavelengths besides the IR, optical, and X-rays. Using radio VLA data, Miller et al. (2005) measured 1.174 ± 0.0085 mJy at 1.4 GHz and 0.677 ± 0.207 mJy at 4.86 GHz. In addition, KWZ measured a V-band magnitude of 22.04 ± 0.08 for the optical counterpart from observations with the Advanced Camera for Surveys (ACS, F550M filter) on the Hubble Space Telescope (HST).

3. SPECTRAL ENERGY DISTRIBUTION (SED)

We construct a base model for the SED of the ULX using the IR, optical, UV and X-ray photometric measurements. The final SED is plotted with the continuous black line in Figure 5. Below we describe in detail the construction of the final SED.

X-ray to UV Band: The UV part of the SED is the most important portion of the SED for our analysis, however it is also unfortunately the most ambiguous. To estimate the UV flux we extrapolated the Modified PLMCD model to lower energies. At lower energies, the MCD can be approximated as a simple power-law with photon index 2/3 (or energy index -1/3, see Mitsuda, et al. 1984). This is because the MCD is a superposition of numerous black bodies representing the integrated emission from the disk at the various temperatures

and radii. At optical energies, this model predicts a drop in flux due to the finite size of the accretion disk (see Fig. 5).

While the MCD accretion disk model is a good approximation of the UV continuum to first order, it does not account for self-irradiation of X-ray photons caused by thickening of the accretion disk at the outer edges and relativistic effects on the X-rays emitted from the inner regions of the disk. In Galactic X-ray binaries, this reflected radiation has been shown to increase the luminosity of the accretion disk by as much as 18% (Sanbuichi et al. 1993; Vrtilik et al. 1990; Revnivtsev et al. 2002). We therefore checked to see if X-ray irradiation would change the ionizing UV emission from the Holmberg II ULX. Following Sanbuichi et al. (1993), we modeled the expected SED of an irradiated disk surrounding black holes with different masses and using different accretion outer radii. Two examples are plotted in Figure 4a. The peak energy here depends primarily on the mass of the BH. For stellar-mass BHs, the irradiated disk peaks in the optical, with very little contribution to the soft UV. For IMBHs, the peak shifts into the IR. A more detailed analysis that takes into account the actual radius of the accretion disk for different stellar companions is presented in Figure 4b. We compare the radius in the disk (R_b) where the reprocessed flux starts to dominate the intrinsic emission with the outer radius of the disk assuming Roche lobe overflow. Irradiation is important only for less massive BHs, even with main sequence companions. However, as can be seen in Figure 4a, the SED at ionizing energies of [OIV] (i.e. the UV SED), is not affected for any size BH relevant to this study, so we will not consider this process further in the photoionization analysis.

Optical Band: The MCD component above was further extrapolated into the optical, where the companion star then dominates the SED (see KWZ). A supergiant B2Ib was first chosen as the optical counterpart in the model, based on the UV photometry. The stellar model is part of the ATLAS9 Model Atmospheres (Castelli & Kurucz 2004), with a temperature of 18500 K and a luminosity of $5 \times 10^{38} \text{ erg s}^{-1}$. Figure 5 shows that the supergiant emits very few photons that can impact the ionization at [OIV] energies. On the other hand, an O5V star (see Fig. 5, also Section 4.3) provides a significant flux above 13.6 eV, but is also significantly deficient above the He II edge.

Infrared and Radio Band: At longer wavelengths, from IR to radio, we use a broken power-law to approximate the SED. These photometric data are viewed as upper limits since the ULX flux is likely contaminated by the surrounding star forming region. We note that the infrared data presented here has little effect on the Cloudy modeling described in Section 4.1 below.

4. CLOUDY SIMULATIONS

4.1. The Base Model

We use the base model described in the previous section as the input ionization source for the Cloudy modeling. Calculations were performed with version 07.02.01 of Cloudy, last described by Ferland et al. (1998). We assume a constant gas density of 10 cm^{-3} (KWZ) and a filling factor of 1. We adopt a spherical geometry for the cloud of gas and assume the inner radius of the cloud to be 0.1 pc, thus maximizing the ionizing flux. The bolometric luminosity extracted from this model is $1.1 \times 10^{40} \text{ erg s}^{-1}$.

To constrain the outer radius of the cloud we compare the predicted radii resulting from matter-bounded and radiation bounded models, and then compare these results with our observations. Using the column densities from the X-ray fits (see Table 1), the matter-bound model predicts an outer radius of only 11 pc. This radius is inconsistent with the 15 and 25 pc radii observed in the He II emission line maps (KWZ).

We therefore started by assuming a radiation-bounded spherical nebula, and ran Cloudy down to a gas temperature of 4000 K. At this temperature the cloud depth is 140 pc, and the column density is $4.2 \times 10^{21} \text{ cm}^{-2}$, more than ten times the X-ray estimated value. The discrepancies between the column densities derived from the X-rays and Cloudy may indicate that both radiation bounded and matter bounded geometries are needed to reproduce the observations. We explore this possibility further in Section 4.4. However, for simplicity we continue with the radiation-bounded geometry in the following analysis.

In Figure 6 we show how the base model incident spectrum is modified after it passes through the cloud. We plot the transmitted spectrum from the Cloudy simulation, including the attenuated incident spectrum and the diffuse emission with the emission lines. The nebular continuum is significant at UV and optical wavelengths. This is consistent with the continuum emission around the ULX seen in the HST image in Figure 1. The nebular contribution to the optical measurement of KWZ is likely small because of the very good resolution of the ACS instrument. However it probably overestimates our UV estimates because of the large extraction region (50 pc). Because of this, we prefer the less luminous stellar counterpart, B2Ib. As we shall see later (Section 4.3), this star also provides a better fit to the data in the Cloudy modeling. As can be seen from a comparison of the X-ray data in Figure 6, the predicted absorption from the radiation bounded model is clearly too large. We also plot the model with ISM grains in Cloudy which approximates the grains in our Galaxy (see Section 4.3). The reddening is clearly seen, with the radiation being re-emitted in far infrared.

The results of the first Cloudy run are given in column 2 of Table 3. The Cloudy predicted values for the Mid-IR lines are close to the observed values. The low ionization lines are the most discrepant. This disparity between the model and the observations for the low and high ionization lines respectively are likely caused by different mechanisms: either observational effects (e.g. sensitivity or aperture effects) or problems with the model parameters (e.g. gas density, metallicity, geometry). In addition, the flux variability of the ULX is also a possible cause. We explore all of these in the following sections.

4.2. Observational Effects

Using the Cloudy output we calculated surface brightness profiles expected for the Mid-IR lines in Table 2, based on the base model. These are plotted in Figure 7. We assume the same spherical geometry and we integrate the emissivity assuming an optically thin gas. A gas density of 10 cm^{-3} was used by KWZ to explain the extent of the He II emission and we adopt this density in our model. As is shown in Figure 7, Cloudy predicts a spatial extent of 20 to 25 pc for the He II which is consistent with the findings of KWZ (15–26 pc). The [O IV] emission from the ULX should be extended to a radius of about ~ 20 pc according to the simulation. Due to the poor resolution of our spectral maps (one LH pixel = 67.5 pc), it is unclear whether the model accurately predicts the spatial extent of the [O IV], but it seems to be consistent with the observations. We note that the surface brightness is also dependent on the filling factor, which was kept to 1 in all simulations.

The disparity between the model and observations for low ionization lines might be explained if the luminosities of the low ionization lines are diminished due to limited sensitivity across the extraction region. Therefore, in Figure 7 we also plot the Cloudy-derived surface brightness profiles for all of the low ionization lines in Table 2 and their sensitivity limits (3-sigma, horizontal lines). Here the sensitivity limits represent the minimum surface brightness that can be expected for each line, and were estimated from the observations. The radius of the 2×2 aperture (of equal area) is shown as a vertical line in this figure. If the luminosities of the low ionization lines were lowered due to sensitivity effects we would expect at least some of the surface brightness predicted by Cloudy to fall below the line sensitivity limit - thus implying that a portion of the flux was not detected. As Figure 7 shows, for [Ne III] limited sensitivity can explain the low values for the observed luminosity. Indeed our observed luminosities are likely deficient by the luminosity predicted between ~ 50 and 80 pc (luminosity obtained by integrating the surface brightness profile from 50 to 80 pc). On the other hand, Cloudy predicts that we are observing all of the [Ne II], [Si II] and [S III] that is produced in our 2×2 aperture, since the minimum observable line

luminosity is well below the predicted profile. Thus for these lines, limited sensitivity cannot explain the observed luminosities and the discrepancy with the Cloudy model.

In addition to sensitivity effects, aperture effects can also cause discrepancies between the observed low ionization luminosities and those predicted from Cloudy. The line luminosities predicted by Cloudy are independent of aperture and represent the maximum line luminosities expected from an input source as described by the base model. However, it is unclear whether excess emission from low ionization lines is missed due to the constraints of our aperture size. If the emission from [Ne II], [Si II], and [S III] is extended beyond the SH aperture, then this could also explain the discrepancy between the Cloudy and observed luminosities.

We conclude that photoionization using the base model is consistent with the *Spitzer* observations of the *high* ionization lines. However, only the [O IV], He II, and [Ne III] lines can be compared reliably with the Cloudy simulation. Indeed, the [O IV] and [Ne III] are the only lines clearly associated with the ULX in our CUBISM maps. However [Ne III] may be contaminated by other sources (see Fig. 2 and Section 2.1 above). A similar result was found by Lehmann et al. (2005) for optical emission lines, where only the He II line was correlated with the ULX. The non-detection of the [Ne V] lines imposes an upper limit to the flux of hard ionizing photons (photons with energy above 97 eV).

4.3. Parameter Study

We investigate here in more detail how the strong radiation from the accretion disk photoionizes the surrounding ISM and produces the observed lines. Starting with the base model in the radiation-bounded geometry, we vary the input parameters to see how they affect the emitted spectrum. We first examine the dependence of the simulated line luminosities (and line ratios) on the X-ray spectrum by changing the MCD disk temperature kT_{in} , the gas density, metallicity and the inner radius of the cloud. We then varied our input X-ray model to include some of the more detailed X-ray models given in Section 2.4. Finally, we explore how the SED of the stellar companion affects the line luminosities and ratios. The models presented are based on the multi-wavelength data of the Holmberg II ULX and the known properties of the surrounding ISM, but this analysis can be applied to ULXs in general.

Varying the Disk Temperature: The disk temperature is first altered by shifting the X-ray base model to lower photon energies, such that the disk luminosity remains constant across the band. As can be seen from Figure 8a, when the disk component peaks at lower energies, the mid-IR emission lines become stronger. For cooler disks (0.1 keV) the [Ne V]

line should be detected in our observations. In contrast, the lower ionization lines are not dependent on the disk temperature over the range usually found in ULXs (0.1–0.5 keV).

Varying the Gas Density of the Cloud: The results obtained by varying the density of the cloud are plotted in Figure 8b. The luminosities and ratios of the lines are not particularly sensitive to gas density (see also KWZ). The [O IV] luminosity increases slightly as the gas approaches the critical density. We estimate a lower limit of $\sim 1 \text{ cm}^{-3}$ on the density from [O IV] spectral maps, however, Figure 8b shows that a lower gas density will only reduce the line luminosity further. The He II line is clearly extended to 15–25 pc (see KWZ) and consistent with a density of $\sim 10 \text{ cm}^{-3}$.

Varying the Metallicity: The dependence of the line luminosities on metallicity is shown in Figure 9a. The [O IV] and [Ne V] line dependence is linear. The predicted line luminosities for a gas with solar abundances are listed in column 6 of Table 3. Interestingly, the base model with a higher input metallicity reproduces the measured [O IV] luminosity in Table 2 very well. In fact a metallicity of $0.19 Z_{\odot}$ (oxygen abundance of 9.3×10^{-5} in absolute value) reproduces the [O IV] to within the calibration error of the instrument, but without increasing the He II, which is already over-predicted in the current version of the model.

Varying the Inner Radius of the Ionizing Cloud: Figure 9b shows that the ionizing power of the incident flux is diluted if the spherical cloud is too far away from the source. If the inner radius is larger than about 10–20 pc, the luminosities of the [O IV] and [Ne V] lines drop dramatically. Interesting, the He II line, though similar to [O IV] in ionization potential, is nearly insensitive to the inner cloud radius. This is likely because the [O IV] and [Ne V] are in a higher stage of ionization than He II and as a result are much more affected by dilution of the ionizing photons (in other words a drop in the ionization parameter) from increasing the inner radius.

Varying the X-ray Source Spectrum: We next change the X-ray part of the source spectrum to the MCDPL model described in Section 2.4. The model is extrapolated to the edge of the [O IV] line as seen in Figure 5. Results from this Cloudy simulation are shown in column 3 of Table 3. The values outputted from this model are clearly not consistent with the measured values. This model predicts a strong [Ne V] line, which is not detected in our *Spitzer* observations, and a He II luminosity 27 times larger than measured by KWZ. The [O IV] flux predicted from this model is also nearly a factor of three larger than the observed flux. We therefore rule out this model. We note that the MCDPL model has been used by many researchers to estimate disk temperatures and even black hole masses. Our findings imply that it is likely not an appropriate model for ULX high-energy spectra.

We also test how sensitive our simulation is to the hard X-rays in the power-law tail, by running the simulation using the MCD component only. The results are listed in column 7 of Table 3. The changes to the expected line luminosities are minor because most of the hard X-ray radiation passes through the gas without any effect on the ionization of the lines.

Varying the Stellar Companion: To test the effect of the stellar companion on the infrared lines we ran the base model with an O5V star replacing the B2Ib supergiant. The temperature and luminosity of the O5V star, 42000 K and 3.2×10^{39} erg s⁻¹, were chosen to match the model used by KWZ. The results (see Table 3) show that the O5V star has a very strong impact on the high ionization lines. The luminosity of the [O IV] line increases by a factor of 3, and the [Ne V] line by factor of 2. If the companion is in fact an O5V star, our measured OM and *GALEX* fluxes are under-luminous and are likely affected by reddening. Inclusion of an O5V star also has a very different effect on the [O IV] versus the He II line. Indeed, the He II luminosity is increased by only 11%. KWZ found a similar result for their model.

The strong impact of the O5V star can be explained if the O star produces copious O⁺⁺ ions (i.p. 35 eV), which are in turn ionized further by the ULX. A comparison between the oxygen ions structure for these models is presented in Figure 11a. The number of photons in the 24.6–54.4 eV interval is three times higher for the O5V star (7.27×10^{48} s⁻¹ compared to 2.42×10^{48} s⁻¹) than the B2Ib supergiant. Figure 11b shows that the local cloud temperature for the O5V star is also about two times higher in the region where the O³⁺ ions are produced (at offsets of 10–20 pc). Indeed, the [O III] $\lambda 5007$ luminosity estimated from Cloudy increases by a factor of six when the O5V star is used instead the B2Ib supergiant.

The companion star therefore has an indirect but strong impact on the [O IV] line emission. A similar effect can be seen on a smaller scale for the [Ne V] line, which has an even higher ionization potential (97 eV). Thus, the [O IV] line does not act simply as a high energy photon counter as is the case with the He II line, but can also provide information about abundances of lower energy photons. This effect can be used to explain the detection of [O IV] in star-forming regions. In this scenario, [O IV] in star forming galaxies can be produced by relatively faint sources of soft X-rays and UV photons hidden in the star forming region, including such sources as ULXs, X-ray binaries, or SNR. This is a significant result, since the origin of [O IV] in star forming galaxies has been the subject of much debate in the literature (Lutz et al. 1998; Schaerer & Stasińska 1999).

Including Dust Grains: Finally we include grains in the surrounding medium, using the ISM grains model in Cloudy, which approximates the grains in our Galaxy. The last column of Table 3 show that Si is depleted significantly in the grains and that the other lines remain about the same as the base models predictions.

4.4. Matter-Bounded Geometry and the Broken Power-Law Model

We verify here that the radiation-bounded geometry is the best geometry for our simulations. While the radiation-bounded simulations fit the data fairly well, they require a column density that is much larger than the values measured from X-ray spectral fits as discussed in Section 2.4. The concern is that the X-ray measurements are strongly dependent on the hardness of the model at low energies. For our base model, the simulation requires a column density of $4.2 \times 10^{21} \text{ cm}^{-2}$, which is more than ten times larger than the measured values from spectral fits (see Table 1).

To make sure a matter-bounded geometry would not yield better results, we ran the base model with a spherical cloud of varying thickness, so that the total hydrogen column fluctuates between 10^{20} and 10^{22} cm^{-2} . These results are plotted in Figure 11a. As discussed in Section 4.1, for a column matching the X-ray fit (the vertical line labeled “Matter Bound”), the nebula is only allowed to be 11 pc in radius. In addition, the predicted fluxes for both [O IV] and He II lines are much lower than the observed values. Clearly this simple matter-bounded geometry is not sufficient to reproduce the observed lines.

As Figure 11a shows, the minimum column density required for the base model to predict the measured values for the high excitation lines is $\sim 5 \times 10^{20}$, or a cloud thickness of 16 pc (the dashed vertical line). Therefore the matter bounded case could work, if the X-ray column density were increased slightly from the X-ray predicted value of 3.26×10^{20} . This would occur if the geometry of the nebulae were asymmetric (i.e. requires both radiation and matter bounded geometries). Indeed, the observations support such a conclusion. KWZ found that to the south and east, He II and $H\beta$ emission suggests a matter-bounded geometry: the low excitation lines are absent here but detected in the west at larger offsets. Our CUBISM maps in Figure 2 have a much lower spatial resolution than the Hubble images, but the [O IV] map suggests a similar geometry to KWZ. The SH maps of [Ne III] and [S III] show that the emission is stronger 50–100 pc west of the ULX. In other words, to the east and south the nebula shows only high excitation lines, while in the west, lower excitation lines are detected. The fact that the low-ionization line luminosities predicted by the matter-bounded models are much lower than the ones predicted by the radiation-bounded geometry offers an easy explanation for the large discrepancies between the Cloudy predictions and our measurements for these lines. For some of these lines we saw in Section 4.2 that sensitivity effects can also play a role.

We checked to see if the broken power-law model would improve the case for a matter-bounded geometry further. The broken power-law model allows for variations in the absorption column, that the base model does not permit, to fit well both the X-ray and the Mid-IR data. A subset of the broken power-law fits are shown in Figure 6. We re-ran our Cloudy

simulation for these models with the corresponding column densities from the X-ray fits. The results are plotted in Figure 11b. The model based on the best fit broken power-law (BFBP) X-ray model (see Table 1) is shown as a vertical line in Figure 11b. The predicted line luminosities for the BFBP-based model are given in Table 3. With this BFBP-based model, the predicted low-ionization line luminosities are much fainter than the observed values, even for the largest column density ($9.2 \times 10^{20} \text{ cm}^{-2}$, assuming a gas density of 10 cm^{-3} , yielding a 29.7 pc cloud radius). On the other hand, the high ionization lines are consistent with the observations.

For the BFBP-based model, the cloud radius is 17.7 pc, which is consistent with the size of the nebula found by KWZ in the east and south. The other tested broken power-law models are compatible with the X-ray data. However they do not match our observed mid-IR line luminosities. We therefore rule these out as possible models for the ionizing radiation. We note that while the BFBP-based model replicates the X-ray data very well, it does not fit the low-ionization spectra. This could result from limited sensitivity as discussed in Section 4.2 or just simply because the low-ionization lines measured are not actually produced by the ULX.

5. SHOCK MODELS

We check to see if shocks might be responsible for the observed mid-IR line luminosities. Indeed, a combination of X-ray photoionization and shocks was recently proposed to explain the morphology of optical lines observed in the vicinity of LMC X-1 (Cooke et al. 2007). In this case the shocks are likely driven by a jet. Abolmasov et al. (2007) performed optical spectroscopy on eight ULXs with nebular counterparts, including the Holmberg II ULX, and found evidence for shocks in all cases based on the $[\text{S II}] \lambda\lambda 6717, 6731/\text{H}\alpha$ ratio. However, using high-excitation lines such as He II and $[\text{O III}]$, these authors also found that Holmberg II ULX and three other ULXs required photoionization to explain the optical ratios.

Lehmann et al. (2005) found evidence of radial velocity variations of $\pm 50 \text{ km s}^{-1}$ from a region similar of size to the He III nebula. It is therefore possible that part of the ionization is caused by shocks. Lutz et al. (1998) noted that modest velocity shocks of $100\text{--}200 \text{ km s}^{-1}$ can produce significant $[\text{O IV}]$ emission. However, when we also take into account the optical data, and in particular the detection of the He II recombination line, our data provide strong evidence *against* shocks as the source of the $[\text{O IV}]$ emission. This is primarily because the He II is not easily produced by shocks. Instead, the simultaneous detection of these lines argues for the presence of significant radiation over the He II edge (see also Schaerer & Stasińska 1999), and therefore suggests photoionization as the most likely line production

mechanism.

To see if shock models could explain the mid-IR line luminosities and ratios observed in Holmberg II, we used Mappings III grids from Allen et al. (2008) to construct diagnostic diagrams. The predicted [O IV] emission from shocks is shown in Figure 12a. We show both pure shocks and shocks with ionized precursors at a gas density of 1 cm^{-3} , and metallicity $0.1 Z_{\odot}$. For these models, the parameters varied are the shock velocity and the “magnetic parameter” $B/n^{1/2}$, where B is the magnetic field and n is the gas density (Dopita & Sutherland 1996). The CUBISM measured flux from the brightest pixel in the [O IV] map is shown as a horizontal line across the plot in Figure 12a. We note that this is not the maximum intensity of the line, and in fact is likely a lower-limit. Indeed the [O IV] emission is not spatially resolved and the quoted value is actually an average over the size of the LH pixel (67.5 pc), rather than the maximum from each of the averaged slits. In spite of this, the value plotted in Figure 12a requires significant shock velocities and such velocities ($> 200 \text{ km s}^{-1}$) were not detected (Lehmann et al. 2005).

For optical lines we chose the He II and the [O III] $\lambda\lambda 4363, 5007$ lines, as per Evans et al. (1999). The ratio [O III] $\lambda 4363$ / [O III] $\lambda 5007$ is sensitive to the gas temperature. Using the data from Lehmann et al. (2005) we calculated the ratio [O III] $\lambda 4959$ + [O III] $\lambda 5007$ / [O III] $\lambda 4363 = 50$, and estimate a temperature of 17800 K (Osterbrock & Ferland 2006). This is consistent with the temperature of the gas in the region of the cloud where O^{++} ions are produced (see Fig. 11b). For the He II/ $\text{H}\beta$ ratio we chose an average (0.2) between the measurements of KWZ, Pakull & Mirioni (2002), and Lehmann et al. (2005). The shock grids for the optical lines are plotted in Figure 12b. For comparison we over plotted the published data for two other ULXs with detected nebulae, Holmberg IX ULX and MF16 in NGC 6946 (Abolmasov et al. 2007). While the Holmberg IX ULX data is consistent with shocks with modest velocities ($< 100 \text{ km s}^{-1}$), Holmberg II ULX and MF16 seem to require very high velocities. Even for the shock plus precursor models, velocities in excess of 300 km s^{-1} are required to reproduce the observed line ratios. Photoionization models are however compatible with the optical data as well, and are also plotted in Figure 12b. These were obtained with Mappings III (version r). We used the base model and the same parameters and conditions as in the Cloudy runs. For photoionization grids, we varied disk temperatures and densities as in Section 4.3.

In summary, some contribution from shocks to the high excitation lines detected from Holmberg II ULX cannot be ruled out completely. However, if there is some contribution from shocks to the high ionization emission line luminosities, it is likely very small, since both He II and [O IV] lines require shocks with velocities in excess of 200 km s^{-1} .

6. OBSERVATIONAL RESULTS

The infrared [O IV] line (together with [Ne V]) is a signature of high excitation usually associated with actively accreting black holes (e.g. Lutz et al. 1998). This line is often used to disentangle the starburst emission in composite type galaxies (Genzel et al. 1998; Sturm et al. 2002; Satyapal et al. 2004; Smith et al. 2004; Satyapal et al. 2007; Meléndez et al. 2008). Moreover, Dasyra et al. (2008) found a good correlation between the luminosity of the [O IV] line and the mass of the central BH in standard AGN. We estimate a BH mass of $3.5 \times 10^4 M_{\odot}$ if this correlation is extrapolated to the Holmberg II ULX.

Genzel et al. (1998) and Sturm et al. (2002) have used the ratio of [O IV]/[Ne II] to distinguish starburst and AGN dominated galaxies in the mid-IR. They find that the ratio [O IV]/[Ne II] for AGN dominated galaxies is generally greater than 1, while starbursts have ratios closer to 0.01. The lower limit of this ratio for the Holmberg II ULX is 1.15, indicative of high excitation, similar to AGN. Other infrared line diagnostics have been proposed by Dale et al. (2006) to disentangle AGN type ionizing sources from star formation. They found that Seyfert galaxies have ratios $[S\ III] \ 33.48 \ \mu m / [Si\ II] \ 34.82 \ \mu m < 0.5$ and $[Ne\ III] / [Ne\ II] > 2$. For the Holmberg II ULX, these ratios (< 0.2 and > 2.0 , respectively) place it well within the Seyfert regime in the Dale et al. (2006) diagnostic diagrams.

7. SUMMARY OF THE MAIN RESULTS

We find that the *Spitzer* observations of Holmberg II ULX and especially the detection of the [O IV] line is consistent with photoionization by the ULX. Of all the lines examined, only the [O IV] line is shown to be clearly correlated with the ULX. However some contribution by the ULX to the [Si II], [S III] and [Ne III] emission line flux is also likely. A summary of our main results is given below.

7.1. Modeling Results

The Base Model (Modified PLMCD): The Cloudy simulations show that the *Spitzer* spectrum is consistent with photoionization by the accretion powered emission from the ULX. We find that limited sensitivity can explain the relatively low fluxes observed for at least [Ne III] compared with predictions for this observation. The base model predicts a slightly lower [O IV] luminosity than the measured values for the radiation-bound case (Table 2), and even lower for the matter-bounded case (Figure 11a). Previous X-ray results have shown that the accretion disk temperature is likely lower than in our base model

(KWZ obtained ~ 0.2 keV). Such disk temperature will increase the predicted line luminosity to match our measurements (Fig. 8a). In addition, a slightly higher metallicity ($0.2 Z_{\odot}$) can yield better fits to both the [O IV] and He II data for this base model. This is because the He II line is already over-predicted and raising the metallicity will not increase this discrepancy (Fig. 9a).

A solar metallicity as obtained by Winter et al. (2007) predicts a [O IV] line too strong compared to our observations. We note that the line luminosities are determined by the *time-averaged* emission from the ULX. Holmberg II ULX has been seen in a low state, with a luminosity less than half the typically reported luminosity (Dewangan et al. 2004). To be consistent with our observations, and with a solar metallicity, the duty cycle for the ULX should be as low as 10–20%, but this has not been observed in X-ray observations since *ROSAT*.

For this model we prefer therefore the scenario of a relatively steady emission rate from the ULX over the past ~ 100 years (as opposed to a highly variable state), but with a slightly higher metallicity ($0.2 Z_{\odot}$, or oxygen abundance 9.3×10^{-5}). In support of this, a metallicity of 0.17 was measured by Pilyugin et al. (2004). We note that while this model reproduces the spectra very well, it requires absorbing columns in the X-rays that are inconsistent with the observations.

PLMCD-Based Model: We find that the widely used PLMCD model, when extrapolated to the UV, is *not* consistent with the observations. The high excitation lines predicted using this model are at least ten times larger than observed. In this case lowering the metallicity to match the [O IV] will not work, because He II will still be much over-predicted. This model has been used extensively to model the X-ray data from ULXs, and sometimes used to find evidence for IMBHs (“cool disks” Miller et al. 2004). More recently this model has been used with more caution (Berghea et al. 2008), but we have shown that this model is inconsistent with the *Spitzer* observations of the Holmberg II ULX.

Matter vs. Radiation Bounded Geometry: The intensity and morphology of the IR lines provides spatial information about the emission line nebula around the Holmberg II ULX. The geometry consistent with our infrared data (and previously published optical data) is approximately spherical but not symmetrical. The CUBISM maps show that to the east and south the nebula shows only high excitation lines that are likely matter-bounded, while in the west, the detection of lower excitation lines might suggest a radiation-bounded cloud. However, observational effects, such as aperture and sensitivity effects, preclude any definitive conclusion on this model. The discrepancies found in Section 2.4 between the Cloudy model and the measured values for the low-excitation lines suggest that the matter-bounded geometry is at play at least in part (probably to east and south as found from

the spectral maps). Moreover, the absorption measurements from the X-ray data require the cloud to be at least matter-bounded toward our line of sight. Therefore, we find that both matter bounded and radiation bounded geometries are likely at work to describe the observed spectra in both the Mid-IR and X-rays.

Shock Models: The shocks models for both IR and optical emission lines show that shocks with velocity $>200 \text{ km s}^{-1}$ are required to generate both the He II and [O IV] lines observed in Holmberg II. The detected radial velocity variations around the ULX are of the order of $\pm 50 \text{ km s}^{-1}$ (Lehmann et al. 2005). Contribution from shocks to these lines is therefore likely to be small.

True X-ray Luminosity: The ULX luminosity estimated using photoionization modeling is independent of the empirical X-ray estimate, which can be affected by both absorption and beaming (King et al. 2001). The nebular emission line luminosities, on the other hand, are time-averaged true luminosities and can provide information about the geometry of emission and the surrounding ISM.

It is now widely accepted that ULXs are variable on timescales from days to years. These timescales are much shorter than the ionization equilibrium timescales in the nebula. Chiang & Rappaport (1996) investigated time-dependent photoionization of H and He for supersoft X-ray sources. The He II ionization equilibrium at the 90% level is reached in $\sim 0.7 \tau_R$ after source turn-on, where $\tau_R = 3000 \text{ yr}$ is the recombination time for He^{++} from KWZ. For periodic sources, it was found that the He II line luminosity decreases significantly with increasing source period. For example, for a period of $10 \tau_R$ and a duty cycle of 10%, the estimated luminosity is 4.7% of that expected from a steady source with the same peak luminosity. That is a 53% deviation from a linear scaling law (10% of the steady state).

This implies that if the Holmberg II ULX is variable, the estimates of KWZ based on the He II line are actually lower limits of the time-averaged luminosity. For O^{+3} , the recombination time is shorter, $\tau_R \approx 100 \text{ yr}$ (Osterbrock & Ferland 2006), for the same ionization conditions: electron density 10 cm^{-3} and temperature 20000 K. We expect therefore that the [O IV] line reaches equilibrium in a shorter time ($< 100 \text{ yr}$), but still long enough to provide a time-averaged estimate of the true luminosity of the ULX.

Finally, the morphology of the emission lines, from both the previously published optical data and our IR data suggest emission that is nearly isotropic, being inconsistent with narrow beaming. Moreover, photoionization modeling with our base model is consistent with the detected high ionization lines, the true bolometric luminosity of this model is $> 10^{40} \text{ erg s}^{-1}$. This is well above the Eddington luminosity for a stellar-mass BH. In addition, some observational results indicate that the BH in Holmberg II is likely much larger than a

stellar mass black hole (see description below).

7.2. Observational Results

Impact on IR Studies of Starbursts: We find that the predicted [O IV] line luminosity is significantly affected by the type of the companion star. Faint [O IV] has been detected in many starbursts and star-forming regions, but its origin is still under debate. Our analysis provides some explanation for this emission, suggesting that the [O IV] line could be produced by relatively faint X-ray sources including X-ray binaries, SNR or ULXs in starburst galaxies.

Observational Properties of the Black Hole: The Mid-IR line ratios that we observe in Holmberg II are consistent with ratios observed in many standard AGN. Indeed we find a [O IV] / [Ne II] ratio comparable to AGN from Sturm et al. (2002). In addition the [S III] / [Si II] ratio for this object places it well within the Seyfert region of Dale et al. (2006).

The bolometric luminosity of the base model is $1.11 \times 10^{40} \text{ erg s}^{-1}$. For accretion within the Eddington limit, the mass of the central BH is at least $85 M_{\odot}$. The estimate based on the inner disk temperature (0.38 keV) in the MCD model gives a much larger mass, $994 M_{\odot}$. Finally, scaling from AGN estimates, the [O IV] emission predicts a mass as large as $10^4 M_{\odot}$. While our analysis excludes strong beaming in Holmberg II ULX, a sub-Eddington IMBH or a super-Eddington stellar-mass BH are both plausible ionization mechanisms that stem from our analysis. Given the X-ray spectral analysis in the literature, and our results that suggest that the ULX has maintained a high luminosity over timescales $> 100 \text{ yr}$, we prefer the IMBH scenario. However, our Cloudy modeling results alone cannot discriminate between these two sources or the two black hole estimates, since we have no way of constraining the accretion rate.

C. T. B. is grateful to Lisa Winter for allowing us to use the processed *XMM-Newton* data. He thanks Richard Mushotzky and Lisa Winter for helpful discussions, and Nicholas Sterling and Marcio Meléndez for their help with Cloudy. R. P. D. gratefully acknowledges financial support from the NASA Graduate Student Research Program.

REFERENCES

- Abolmasov, P., Fabrika, S., Sholukhova, O., & Afanasiev, V. 2007, *Astrophysical Bulletin*, 62, 36
- Allen, M. G., Groves, B. A., Dopita, M. A., Sutherland, R. S., & Kewley, L. J. 2008, *ApJS*, 178, 20
- Begelman, M. C., King, A. R., & Pringle, J. E. 2006, *MNRAS*, 370, 399
- Begelman, M. C. 2002, *ApJ*, 568, L97
- Berghea, C. T., Weaver, K. A., Colbert, E. J. M., & Roberts, T. P. 2008, *ApJ*, in press
- Bianchi, L., Madore, B., Thilker, D., Gil de Paz, A., & Martin, C., 2005, in “The Local Group as an Astrophysical Laboratory”, ed. M. Livio & T. M. Brown (Cambridge: Cambridge Univ. Press)
- Castelli, F., & Kurucz, R. L. 2004, *ArXiv Astrophysics e-prints*, arXiv:astro-ph/0405087
- Chiang, E., & Rappaport, S. 1996, *ApJ*, 469, 255
- Colbert, E. J. M., & Mushotzky, R. F. 1999, *ApJ*, 519, 89
- Cooke, R., Kuncic, Z., Sharp, R., & Bland-Hawthorn, J. 2007, *ApJ*, 667, L163
- Dale, D. A., et al. 2006, *ApJ*, 646, 161
- Dasyra, K. M., et al. 2008, *ApJ*, 674, L9
- Dewangan, G. C., Miyaji, T., Griffiths, R. E., & Lehmann, I. 2004, *ApJ*, 608, L57
- Dopita, M. A., & Sutherland, R. S. 1996, *ApJS*, 102, 161
- Evans, I., Koratkar, A., Allen, M., Dopita, M., & Tsvetanov, Z. 1999, *ApJ*, 521, 531
- Fabrika, S. 2004, *Astrophysics and Space Physics Reviews*, 12, 1
- Fender, R., & Belloni, T. 2004, *ARA&A*, 42, 317
- Ferland, G. J., Korista, K. T., Verner, D. A., Ferguson, J. W., Kingdon, J. B., & Verner, E. M. 1998, *PASP*, 110, 761
- Genzel et al. 1998, *ApJ*, 498, 579
- Goad, M. R., Roberts, T. P., Reeves, J. N., & Uttley, P. 2006, *MNRAS*, 365, 191

- Gonçalves, A. C. & Soria R. 2006, MNRAS, 371, 673
- Kaaret, P., Ward, M., & Zezas, A. 2004, MNRAS, 351, L83
- Kennicutt R.C. et al. 2003, PASP, 115, 928
- Kerp, J., Walter, F., & Brinks, E. 2002, ApJ, 571, 809
- King, A. R., Davies, M. B., Ward, M. J., Fabbiano, G., & Elvis, M. 2001, ApJ, 552, L109
- Kuntz, K. D., Harrus, I., McGlynn, T. A., Mushotzky, R. F., & Snowden, S. L. 2008, PASP, 120, 740
- Lehmann, I. et al. 2005, A&A, 431, 847
- Liu, Q. Z., & Mirabel, I. F. 2005, A&A, 429, 1125
- Lutz, D., Kunze, D., Spoon, H. W. W., & Thornley, M. D. 1998, A&A, 333, L75
- Meléndez, M., Kraemer, S. B., Schmitt, H. R., Crenshaw, D. M., Deo, R. P., Mushotzky, R. F., & Bruhweiler, F. C. 2008, ArXiv e-prints, 808, arXiv:0808.4154
- Miller, J. M., Fabian, A. C., & Miller, M. C. 2004, ApJ, 614, L117
- Miller, N. A., Mushotzky, R. F., & Neff, S. G. 2005, ApJ, 623, L109
- Mitsuda, K. et al. 1984, PASJ, 36, 741
- Miyaji, T., Lehmann, I., & Hasinger, G. 2001, AJ, 121, 3041
- Osterbrock D. & Ferland G., Astrophysics of Gaseous Nebulae and active Galactic Nuclei, Second Edition, 2006, University Science Books, Sausalito, California.
- Pakull, M. W., & Angebault, L. P. 1986, Nature, 322, 511
- Pakull, M., & Mirioni, L. 2002, in “New Visions of the X-ray Universe in the XMM-Newton and Chandra Era”, (Noordwijk: ESTEC), (astro-ph/0202488)
- Pilyugin, L. S., Vílchez, J. M., & Contini, T. 2004, A&A, 425, 849
- Poutanen, J., Lipunova, G., Fabrika, S., Butkevich, A. G., & Abolmasov, P. 2007, MNRAS, 377, 1187
- Remillard, R. A., Rappaport, S., & Macri, L. M. 1995, ApJ, 439, 646
- Revnivtsev, M., Sunyaev, R., Gilfanov, M., & Churazov, E. 2002, A&A, 385, 904

- Sanbuichi, K., Yamada, T. T., & Fukue, J. 1993, PASJ, 45, 443
- Satyapal, S., Sambruna, R. M., & Dudik, R. P. 2004, A&A, 414, 825
- Satyapal, S., Vega, D., Heckman, T., O’Halloran, B., & Dudik, R. 2007, ApJ, 663, L9
- Schaerer, D., & Stasińska, G. 1999, A&A, 345, L17
- Smith, J. D. T. et al. 2004, ApJS, 154, 199
- Stobart, A-M., Roberts, T. P., & Wilms, J. 2006, MNRAS, 368, 397
- Sturm, E., Lutz, D., Verma, A., Netzer, H., Sternberg, A., Moorwood, A. F. M., Oliva, E., & Genzel, R. 2002, A&A, 393, 821
- Swartz, D. A., Ghosh, K. K., McCollough, M. L., Pannuti, T. G., Tennant, A. F.; Wu, K. 2003, ApJS, 144, 213
- Vrtilek, S. D., Raymond, J. C., Garcia, M. R., Verbunt, F., Hasinger, G., & Kurster, M. 1990, A&A, 235, 162
- Winter, L. M., Mushotzky, R. F., & Reynolds, C. S. 2006, ApJ, 649, 730
- Winter, L. M., Mushotzky, R. F., & Reynolds, C. S. 2007, ApJ, 655, 163
- Zezas, A. L., Georgantopoulos, I., & Ward, M. J. 1999, MNRAS, 308, 302

Table 1. X-ray model fits

Model (1)	N_H (2) 10^{20} cm^{-2}	kT_{in}/Γ_1 (3) keV	Γ/Γ_2 (4)	$\Delta\chi^2/\text{dof}$ (5)	L (6) $10^{40} \text{ erg s}^{-1}$	MCD flux (7)
Modified PLMCD	3.26 ± 0.56	0.38 ± 0.02	2.54 ± 0.02	1.02/135, 0.974/713	1.11	0.49
PLMCD	10.4 ± 0.70	0.27 ± 0.02	2.42 ± 0.05	1.1386/849	2.28	0.12
BFBP	5.49 ± 0.78	1.73 ± 0.10	2.57 ± 0.02	1.0316/849	1.41	0.60

Note. — (1): X-ray model. (2): Intrinsic hydrogen column density. The Galactic column density from KWZ ($3.42 \times 10^{20} \text{ cm}^{-2}$) was added separately. (3): Inner disk temperature for the MCD component. For the broken power-law model this is the first (low energies) photon index parameter. The break is at 1.0 keV. (4): Photon index for the power-law component. For the broken power-law model this is the second (high energies) photon index parameter. (5): Reduced χ^2 values for the fit and the number of degrees of freedom. For the base model we quote two values for each separately fitted component (see text for details). (6): Unabsorbed (intrinsic) luminosities between 0.1 and 10 keV. (7): MCD component unabsorbed flux as fraction of the total flux. For the base model and the broken power-law model we simply divided the flux between 0.1 and 1.0 keV to the flux in the whole range (0.1–10 keV)

Table 2. Measured Infrared Lines

Line (1)	SH Aperture			4 Pixels Aperture		
	Flux (2)	S/N Ratio (3)	L (4)	Flux (5)	S/N Ratio (6)	L (7)
[Ne II] 12.81 μm	<6.08	...	<0.68	<1.98	...	<0.22
[Ne III] 15.56 μm	12.15 ± 3.4	4.60	1.35 ± 0.39	5.46 ± 1.37	7.6	0.61 ± 0.15
[S III] 18.71 μm	2.64 ± 1.14	4.64	0.29 ± 0.13	3.02 ± 1.16	4.7	0.34 ± 0.13
[Ne V] 24.32 μm	<3.88	...	<0.43	<1.16	...	<0.13
[O IV] 25.89 μm	7.01 ± 1.60	10.16	0.78 ± 0.2	3.63 ± 0.91	44.4	0.40 ± 0.1
[S III] 33.48 μm	<4.39	...	<0.49	<1.53	...	<0.17
[Si II] 34.82 μm	21.91 ± 5.48	9.90	2.44 ± 0.61	5.87 ± 1.47	7.2	0.65 ± 0.16

Note. — We show line fluxes for the largest SH and LH common aperture as defined in Section 2, and for the smallest possible aperture (4 LH pixels) centered at the ULX position. Fluxes are in 10^{-22} W cm^2 , luminosities (L) in $10^{37} \text{ erg s}^{-1}$. If the measurements errors are smaller than the absolute calibration accuracy of 25%, the latter were used. For nondetections we show 3σ upper limits.

Table 3. Predicted Line Luminosities from Cloudy

Line (1)	Base Model (2)	PLMCD (3)	BFBP (4)	O5V Star (5)	Solar abundances (6)	Without PL (7)	Grains (8)
[Ne II] 12.81 μm	1.09	1.81	<0.01	1.10	1.48	1.07	0.55
[Ne III] 15.56 μm	1.02	2.58	<0.01	1.23	3.68	0.99	0.81
[S III] 18.71 μm	1.75	3.86	<0.01	1.82	5.35	1.72	1.24
[Ne V] 24.32 μm	0.15	3.83	0.38	0.32	1.58	0.14	0.14
[O IV] 25.89 μm	0.41	9.31	0.67	1.31	4.41	0.40	0.38
[S III] 33.48 μm	4.38	9.38	<0.01	4.51	13.4	4.29	3.08
[Si II] 34.82 μm	13.43	22.23	<0.01	13.71	18.3	13.21	7.57
He II 4686 Å	0.53	7.26	0.57	0.59	0.53	0.51	0.50

Note. — Predicted line luminosities (in $10^{37} \text{ erg s}^{-1}$) from different Cloudy models: (2): The base model. (3): The two-component MCDPL based model frequently used in fitting ULX X-ray spectra. (4): The best fit broken power-law (BFBP) based model ran with the matter-bounded geometry. (5): Same as the base model but with the supergiant B2Ib replaced by an O5V star. (6): The base model with solar abundances. (7): The base model without the power-law tail. (8): The base model with grains;

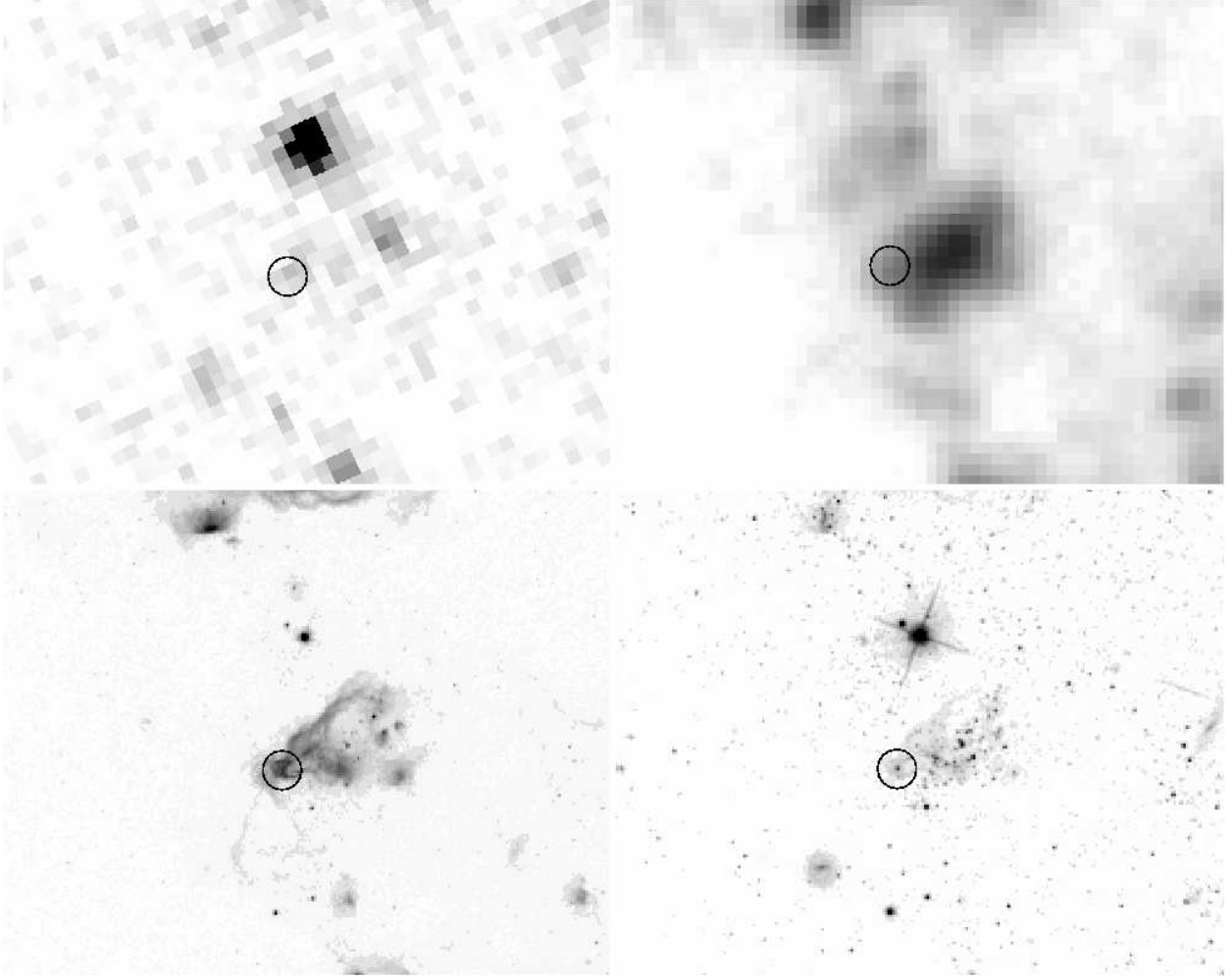


Fig. 1.— Clockwise from top left: *Spitzer* IRAC 8 μ m, XMM-OM UVW1 filter, HST ACS 814W and 658N filters. A 50 pc diameter circle around the ULX position is drawn on all images. This was used as extraction region for photometry measurements in Section 2. North is up, east to the left.

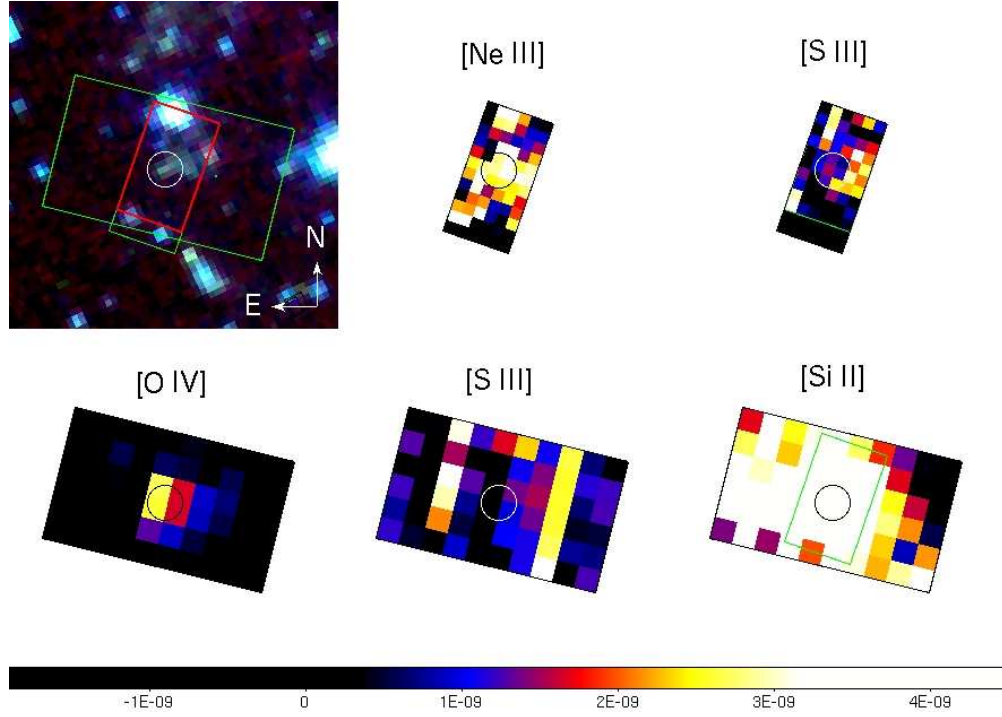


Fig. 2.— Spectral maps for: [Ne III] $15.56 \mu\text{m}$, [S III] $18.71 \mu\text{m}$, [O IV] $25.89 \mu\text{m}$, [S III] $33.48 \mu\text{m}$ and [Si II] $34.82 \mu\text{m}$. The units on the colorbar are $\text{W m}^{-2} \text{sr}^{-1}$. Top left shows an IRAC image with the SH and LH apertures and the common aperture used to extract the spectra (red). We also extracted spectra from the 4 LH pixels that include the 100 pc diameter region (this is shown on all images, as a circle centered on the *Chandra* position) and the 4 LH pixels just below the 100 pc region. The colorbar does not apply to the IRAC image, the colors here are red: $8.0 \mu\text{m}$, green: $4.5 \mu\text{m}$ and blue: $3.6 \mu\text{m}$.

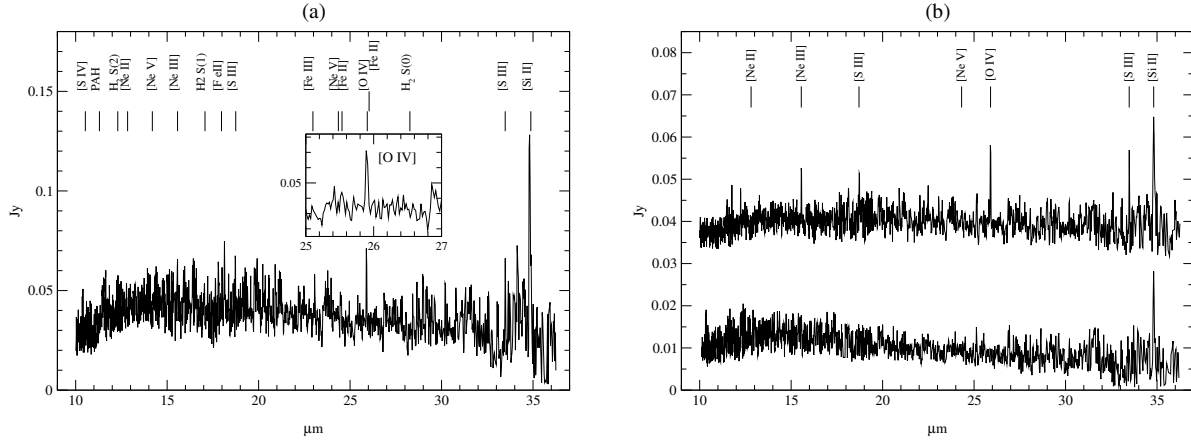


Fig. 3.— Full IRS spectrum obtained from matched apertures with CUBISM. a) The aperture used is the whole SH aperture. The inset shows a zoomed region around the [O IV] line. b) Spectra were obtained from two apertures of 4 LH pixels in size, the top spectrum from the four pixels coincident with the [O IV] line, and below for comparison from the four pixels just below (see the [O IV] map in Figure 1). The [O IV] is clearly concentrated in the four LH pixels aperture.

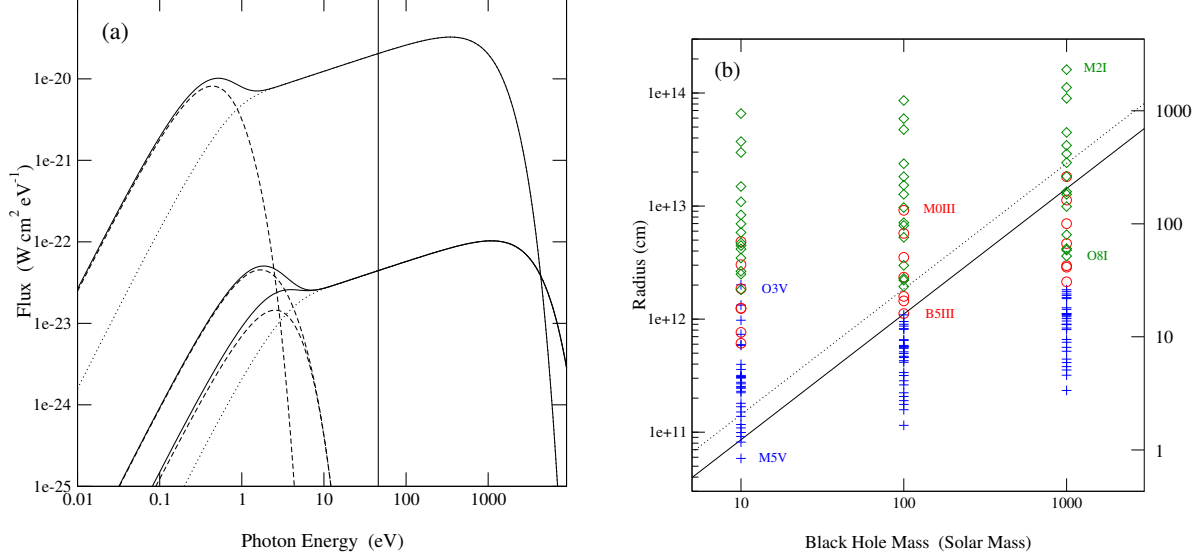


Fig. 4.— a) Examples of irradiated disks spectra. The higher flux spectrum is calculated for a $1000 M_{\odot}$ intermediate-mass BH binary and an outer radius of 10^{14} cm. The lower spectrum is for a stellar-mass BH binary of $10 M_{\odot}$ and two disk sizes: 3×10^{11} cm and 10^{12} cm. The continuous lines show the total spectrum, dotted lines the spectrum from inner disk, not affected by the irradiation, and the dashed lines from the outer part. The vertical line marks the [O IV] ionization edge. The reprocessed photons have energies below 10 eV, and therefore not ionizing. All cases assume accretion at Eddington luminosity. b) Roche lobe sizes compared to radii of the irradiated part of accretion disk. The lines show the radius (R_b) of the accretion disk where the reprocessed irradiation equals the intrinsic emission for different BH masses. The continuous line assumes accretion at Eddington luminosity, while the dotted line is for accretion at 1%. The symbols mark Roche lobe sizes for a combination of BH masses (10, 100 and $1000 M_{\odot}$) and star types. We assume that the companion fills its Roche lobe. Luminosity classes are marked with the following signs: pluses (main sequence), circles (giants) and diamonds (supergiants). For the stars spectral type we only marked the extremes and just once for each BH mass for clarity. On the right Y-axis the units are solar radii. For large BHs the irradiation is only important if the companion is an evolved star.

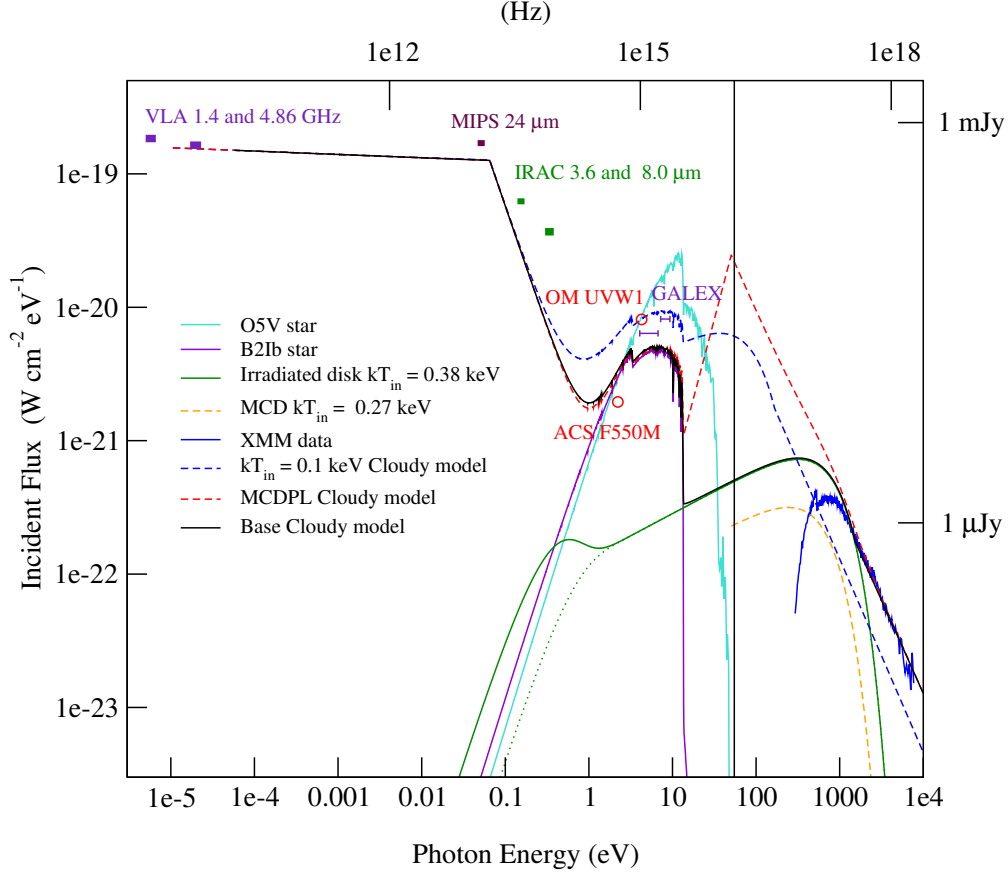


Fig. 5.— This figure shows the SED and models used in Cloudy modeling. The radio data is from Miller et al. (2005), The V-band magnitude for the optical counterpart of the ULX is quoted from KWZ. Our measured fluxes from IRAC, MIPS, OM and GALEX are upper limits, and therefore our model is below these data points. The two stellar spectra correspond to the spectral types range consistent with the colors and magnitudes in KWZ. The X-ray data is from the long (~ 100 ks) *XMM-Newton* observation ID 0200470101. The base model was obtained by fitting the MCD and power-law components separately as explained in the text. The MCDPL model is the popular ULX model, with a cool disk ($kT_{in} = 0.27$ keV) and a power law tail at high energies. The MCD component of this model is also shown separately, for comparison with the MCD in the base model. We extrapolated the MCDPL model only to the [O IV] edge at 54.93 eV (shown as a vertical line). We also show a model obtained from the base model by shifting to lower energies, such that $kT_{in} = 0.1$ keV.

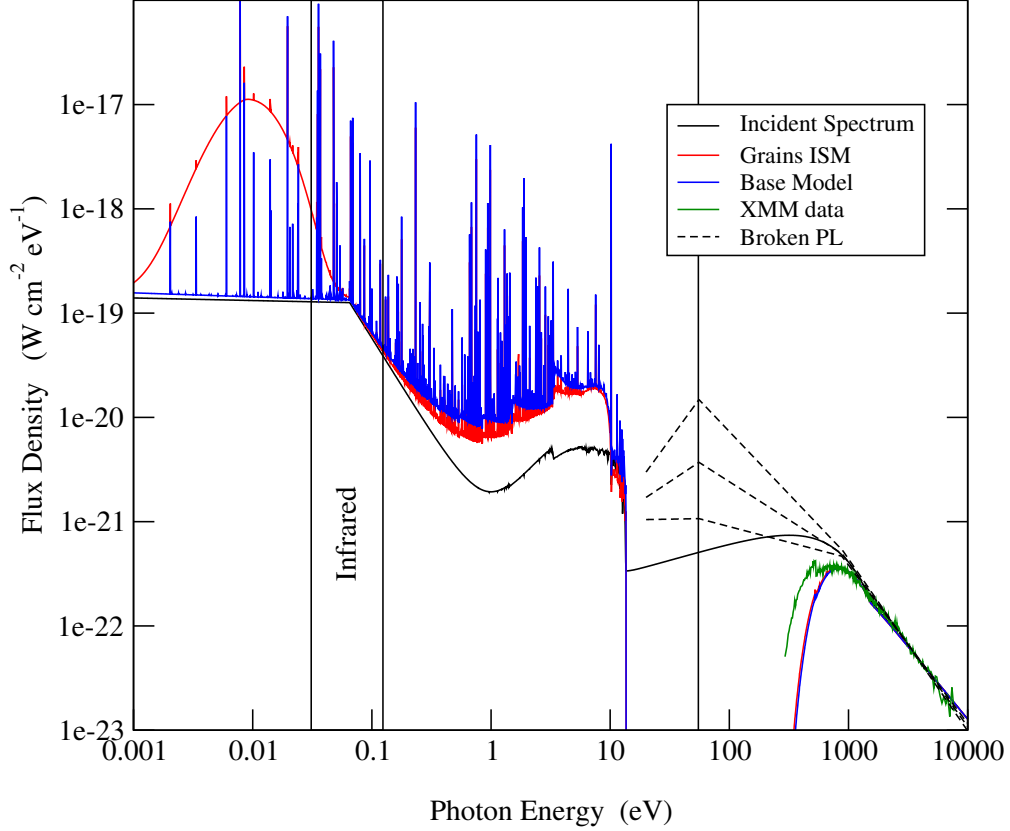


Fig. 6.— Transmitted spectra from Cloudy. We show the transmitted spectrum through the cloud for the base model and for the model with ISM grains in Cloudy. Both spectra include the attenuated incident spectrum and the diffused emission with the emission lines. We also plot the incident spectrum of the base model and the X-ray data. The vertical band labeled “Infrared” shows the *Spitzer* high resolution range: $10\ \mu\text{m} - 40\ \mu\text{m}$. The dashed lines show family of broken power-law models fitted to the X-ray data (see also Figure 11). All the models between the lower ($\Gamma = 1.3$) and upper ($\Gamma = 2.2$) plotted lines are compatible with the X-ray data given the errors. The middle one ($\Gamma = 1.73$) is the best fit broken PL (BFBP) model in Table 3. These models are extrapolated from X-ray to the [O IV] line edge at 54.93 eV (the vertical line), and are only shown down to 20 eV for clarity.

Fig. 7.— Emission lines surface brightness and instrument sensitivity effects. We used the Cloudy results from our base model with a gas density of 10 cm^{-3} . The vertical line marks the size of a circular aperture of area equal to the 4 LH pixel aperture.

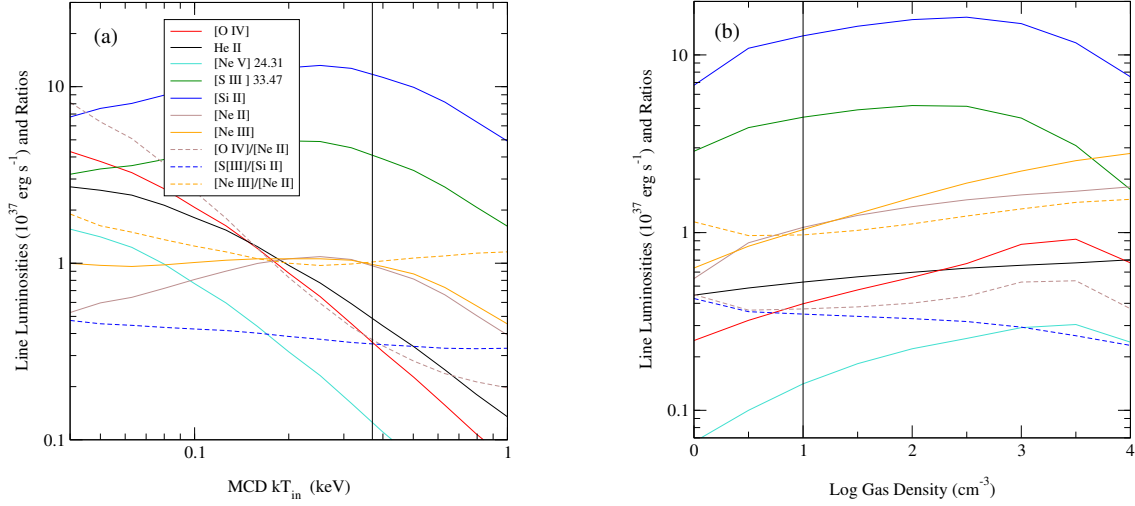


Fig. 8.— The dependence of the simulated lines from Cloudy on: a) MCD inner disk temperature. b) Gas density of the cloud. The vertical lines mark the base model values: $kT_{in} = 0.38$ keV, $\text{density} = 10 \text{ cm}^{-3}$. The line colors are the same but only labeled in the left panel.

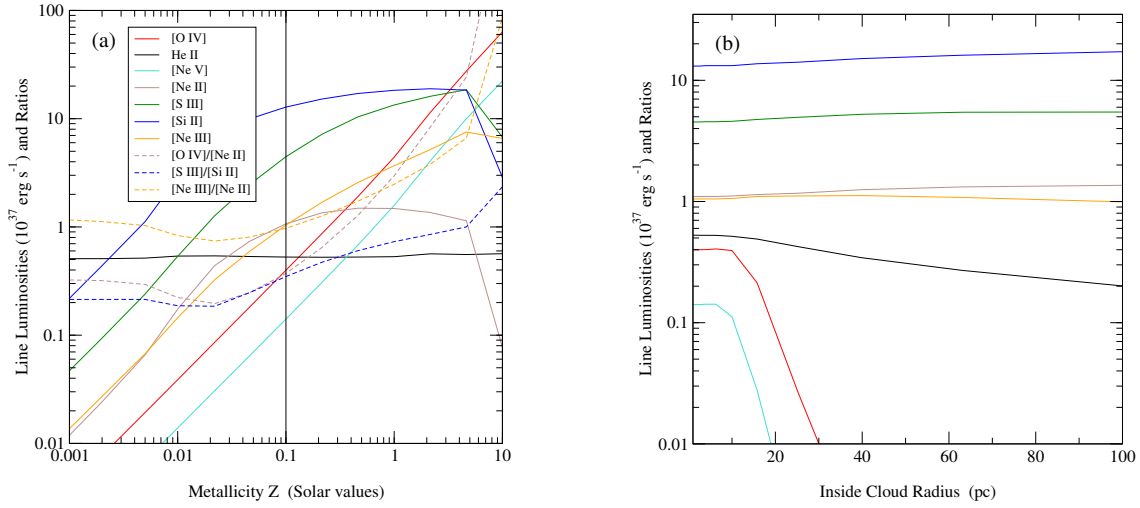


Fig. 9.— The dependence of the simulated lines from Cloudy on: a) Cloud metallicity. b) The inner radius of the cloud. The vertical line marks the base model value of $Z = 0.1 Z_{\odot}$. The line colors are the same but only labeled in the left panel.

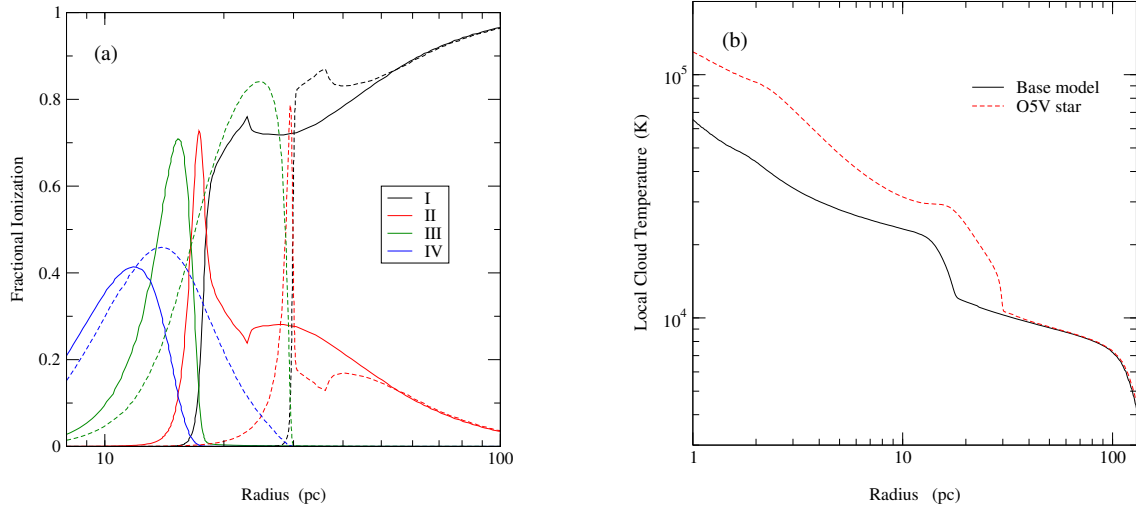


Fig. 10.— Comparison between the base model, with the B2Ib star (continuous line) and the model with the O5V star (dashed line). a) The oxygen ionic structure in the cloud. We only plot the ions up to O^{3+} . b) Local temperature in the cloud.

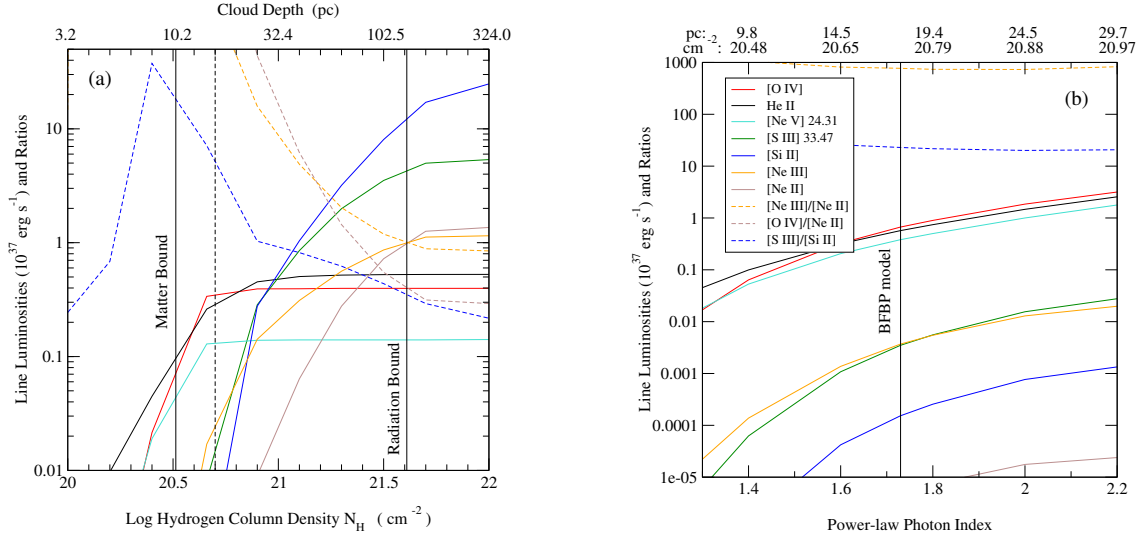


Fig. 11.— This figure illustrates the difference between a matter bounded and radiation bounded nebula. The line colors are shown only in the right panel. The ratio $[\text{Ne III}]/[\text{Ne II}] > 1000$ on the right plot, and is not shown for clarity. a) The dependence of the simulated lines from Cloudy on the cloud hydrogen column density for the base model. The equivalent depth of the spherical cloud is also marked on the top X-axis. Both vertical continuous lines mark the column density for the base model, but one value was obtained by fitting the X-ray data with the base model (matter bounded nebula), while the other is the column in the Cloudy simulation where the local temperature reached 4000 K (radiation bounded). We also marked with a vertical dashed line the limit where the predictions for the high excitation lines are still compatible with observations. b) The simulated lines using the family of broken power-law models fitted to the X-ray data. The best fit broken PL (BFBP-based) model is marked by the vertical line. The bottom X-axis shows the low-energy photon index for the models. On the top X-axis we mark the corresponding log column densities (lower values) and cloud depths (upper values). All these models are matter bounded.

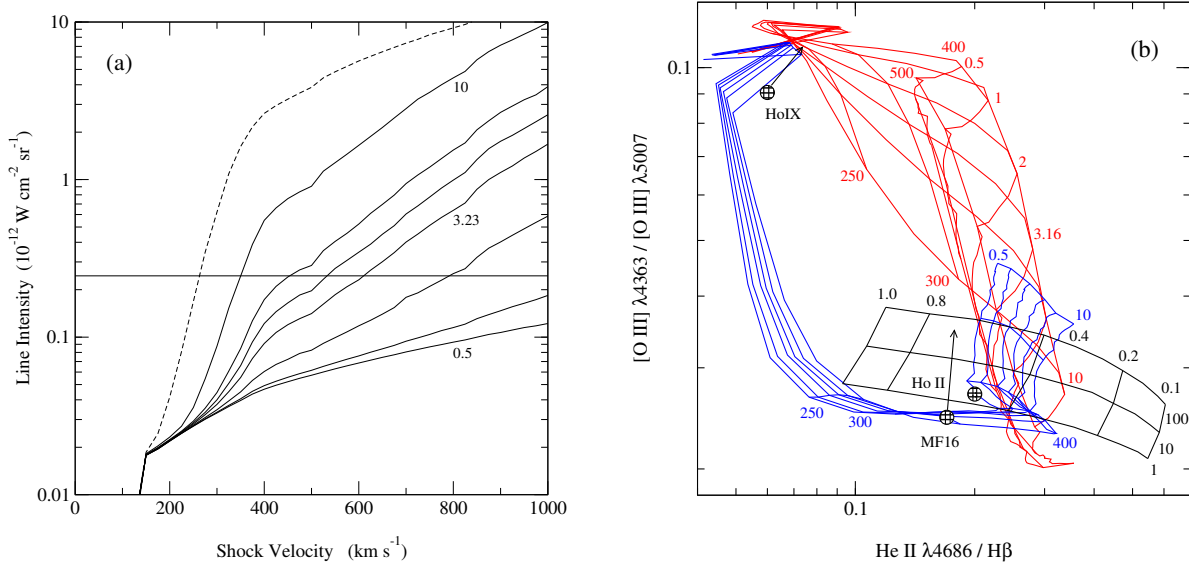


Fig. 12.— Mappings III shocks and ionization models. The shock grids are plotted for magnetic parameters: 0.5, 1, 2, 3.23, 5 and 10 $\mu\text{G cm}^{3/2}$ and for shock velocities 125, 250, 300, 400, 500, 700 and 1000 km s^{-1} . a) [O IV] line intensity shocks predictions. The shocks plus precursor models vary little with the magnetic parameter, and we only show the model with a nominal equipartition value (3.23 $\mu\text{G cm}^{3/2}$, the dashed line). The horizontal line shows the CUBISM lower limit value of $2.45 \times 10^{-13} \text{ W cm}^{-2} \text{ sr}^{-1}$. b) Optical lines diagnostic with shocks and photoionization models. The pure shock models are in red, shocks plus precursor in blue and the photoionization grid in black. For the photoionization grid we varied the density (1, 10 and 100 cm^{-3}), and the inner disk temperature (0.1, 0.2, 0.4, 0.8 and 1.0 keV), and assumed a metallicity of 0.1 Z_{\odot} . For Holmberg IX ULX and MF16 we show with arrows the approximate locations for Solar metallicity. While Holmberg IX ULX is consistent with shocks with modest velocities ($< 100 \text{ km s}^{-1}$), Holmberg II ULX and MF16 seem to require very high velocities. They are however consistent with photoionization.